RSC Advances

PAPER

View Article Online
View Journal | View Issue

Cite this: *RSC Adv.*, 2024, **14**, 16971

In situ fabrication of Fe_3C nanoparticles and porous-carbon composites as high-performance electromagnetic wave absorber†

Wentao Yu, [a] Jiahui Lin,[a] Yan Cao,[a] Jiyong Fang, [b] Ziqing Wang, [c] Jintao Huang *[a] and Yonggang Min *[a]

Received 12th February 2024
Accepted 2nd April 2024

DOI: 10.1039/d4ra01093k

rsc.li/rsc-advances

This study successfully utilized a straightforward approach, choosing liquid–liquid phase separation to build a porous structure and synthesize composite absorbers based on polyimide-based porous carbon/Fe_3C (PIC/Fe_3C-1, PIC/Fe_3C-2) nanoparticles and porous carbon/FeCo alloy nanoparticles (PIC/FeCo). The specially designed network structure pore structures contributed multiple reflection, conduction loss and strong interfacial polarization. After characterization, PIC/Fe_3C-2 obtained minimum RL of −35.37 dB at 17.04 GHz with 1.55 mm thickness and effective absorption bandwidth of 4.95 GHz with 1.66 mm thickness. Furthermore, PIC/FeCo, with a thickness of 1.63 mm, exhibits the most robust electromagnetic wave loss ability at 15.6 GHz, with a minimum RL of −56.32 dB and an effective absorption bandwidth of 4.88 GHz. Thus, the design strategy presented in this study could serve as a model for synthesizing other high-performance absorbers, effectively mitigating electromagnetic wave-induced pollution.

Introduction

With the development of 5G communications and the unrestricted use of electronic products, the public is deeply concerned about the resulting electromagnetic wave (EMW) pollution.[1–3] On the one hand, long-term exposure to EMW radiation has harmful effects on human health; on the other hand, EMW radiation causes damage to electrical equipment, shortening its service life. Therefore, there is increasing interest in seeking effective methods to mitigate or eliminate the adverse effects associated with EMW pollution. Current research suggests that effective EMW wave shielding can be facilitated by utilizing EMW-absorbing materials capable of converting residual EMW into thermal energy (rather than merely reflecting thermal energy).[4–6] This methodology contributes to the prevention of secondary EMW pollution, thereby enhancing the efficiency of EMW utilization. The utilization of EMW absorption materials emerges as a viable prospect. Consequently, the advancement of EMW absorption materials has emerged as a pivotal focal point in the realm of EMW protection.

In a general context, outstanding EMW absorption materials exhibit robust EMW attenuation capabilities, a broad effective absorption frequency bandwidth, lightweight structures, and thin thicknesses, with these characteristics varying based on distinct application conditions.[7–9] Numerous compounds can function as ideal EMW-absorbing material. Traditional EMW-absorbing materials included magnetic metal (Fe, Co, Ni),[10–12] their oxide (*e.g.* Fe_3O_4, $CoFe_2O_4$ and NiO)[13–16] and carbon composites (*e.g.* graphene, RGO, CNT).[17–20] Compared with metal composites, carbon materials exhibit unique properties in EMW absorption applications, including lighter weight, higher electrical loss, and good chemical stability. However, to obtain exceptional EMW absorption performance, not only require the presence of strong dielectric loss, but also electromagnetic impedance matching conditions.[21] Any single carbon material, which rely solely on dielectric loss and exhibit low impedance matching, are not viable options for EMW absorption. Instead, introducing magnetic materials or another dielectric material into carbon materials to prepare composite materials. It is an effective way to overcome the limitations of carbon-only materials and offer a feasible solution to achieve fine EMW absorption performance. For example, Sun *et al.* prepared carbon nanofibers embedded by a-Fe_2O_3, Fe and Fe_3C nanocrystals (Fe_3C/C, a-Fe_2O_3/C, Fe/C) through carbonization in different atmospheres. Fe_3C/C exhibited a minimum reflection loss value of −57.9 dB at 4.10 mm.[22] Wang *et al.* prepared lightweight multifunctional PDMS/Fe_3O_4/CF through high-temperature pyrolysis and dip coating process. The sample demonstrated a minimum RL value of −47.36 dB at a thickness

[a]*Department of Polymer Materials and Engineering, School of Materials and Energy, Guangdong University of Technology, Guangzhou 51006, China. E-mail: jintao.huang@gdut.edu.cn; ygmin@gdut.edu.cn*

[b]*Midea Corporate Research Center, Foshan 528000, China*

[c]*Visionox Technology Co., Ltd, Guangzhou 51000, China*

† Electronic supplementary information (ESI) available. See DOI: https://doi.org/10.1039/d4ra01093k

of 3.15 mm and an effective bandwidth of 9.76 GHz at a thickness of 4.2 mm.[23] However, introducing magnetic metal materials may lead to an increase in composite material density and potentially have adverse effects on impedance matching.

The incorporation of hollow or porous structures into absorbers not only reduces their weight but also enhances their specific surface area and transmission efficiency. Furthermore, including low-dielectric air in the material leads to improved impedance matching. Previous studies have extensively explored porous or core–shell structures in this domain.[24–27] Qiang *et al.* designed and synthesized a unique microstructure that endows yolk–shell C@C microspheres.[28] The synthesized yolk–shell C@C exhibited outstanding EMW absorption performance, with a minimum RL of −39.4 dB. Overall, creating porous structures plays a crucial role in EMW absorption performance. However, the complex design and manufacturing of porous structures have posed challenges to their industrial production. Therefore, there is an urgent need for a simple and controlled synthetic method to design carbon/magnetic metal composite materials with porous or hollow structures as novel EMW absorbers.

This study delineates a straightforward and effective approach for fabricating porous carbon/cobalt nanoparticle EMW absorbers utilizing a one-step pyrolysis and liquid–liquid phase separation (LLPS) technique. As previously reported, the selection of polyimide (PI) as the carbon precursor stems from its outstanding thermal stability and amendable characteristics for modification.[29–31] In our previous work, we demonstrated that PI-derived porous carbon prepared *via* LLPS maintains its porous structure during pyrolysis and revealed that increasing carbonization temperature impacts EMW absorption performance.[32] Herein, to further explore the conformational relationship between the types, contents, and morphology of nanoparticles and their EMW absorption performance, we varied iron acetylacetonate and acetylacetone cobalt(III) as the magnetic nanoparticles source, incorporating it into a polyamic acid solution through rapid stirring to form the composite material precursor. After LLPS treatment and high-temperature pyrolysis, the porous carbon/Fe_3C (PIC/Fe_3C) and porous carbon/FeCo alloy (PIC/FeCo) composite absorbers were prepared. Systematic characterizations were performed on the internal composition, microscopic morphology, and EMW absorption capabilities of PIC/Fe_3C and PIC/FeCo. "As exceptional absorbers, the structural and compositional advantages of PIC/Fe_3C and PIC/FeCo lie in their abundant porous structure and various polarization effects, including interface polarization, defect polarization and dipole polarization. Consequently, this work provides a straightforward and feasible pathway for the large-scale synthesis of carbon-based EMW absorbers, replicable with high fidelity.

Experiment

Materials

Dimethylacetamide (DMAC), iron acetylacetonate ($Fe(acac)_3$) and acetylacetone cobalt(III) ($Co(acac)_3$) were supplied by Aladdin Chemistry Co. Ltd and used without further purification. 4,4′-Oxydianiline (ODA) and Pyromellitic dianhydride (PMDA) were supplied by Macklin Co. Ltd and used as received. Deionized water was used throughout the experiments.

Synthesis of polyamicacid (PAA) precursor solution

Firstly, 20 g ODA was added into 137 g DMAC and stirred for an hour at 25 °C. Second, 23 g PMDA were slowly added after the diamine had dissolved completely. The solution was stirred at 25 °C for 6 h to obtain a PAA precursor solution.

Preparation of porous PI/Fe $(acac)_3$ composites (PI/Feac-1, PI/Feac-2) and PI/Fe $(acac)_3$/$Co(acac)_3$ composites (PI/Feac/Coac)

Firstly, 10.0 g of DMAC and 1.67 g of $Fe(acac)_3$ were added to 30.0 g PAA solution and stirred for an hour at 25 °C. Second, the above solution was scraped the film with a coating rod on a glass plate and formed a uniform solution membrane. Then, the obtained solution membrane was immediately immersed in a coagulation bath filled with deionized water at 25 °C for 24 h. Thus, the obtained membrane was dried at 70 °C for 24 h. Third, the dried porous PAA membrane was imidization in a baking oven under specific heating conditions: 150 °C/1 h; 250 °C/1 h; 350 °C/1 h. Then, the obtained porous polyimide/$Fe(acac)_3$ composite membrane was labeled as PI/Feac-1. By changing the additional amount of $Fe(acac)_3$ to 3.34 g, the composite membrane obtained were was labeled as PI/Feac-2.

The whole preparation process of PI/Fe $(acac)_3$/$Co(acac)_3$ composite membrane is basically the same as that of PI/$Fe(acac)_3$. When the 1.67 g of $Fe(acac)_3$, 1.67 g of $Co(acac)_3$ were added to 30.0 g PAA solution, the composite membrane obtained was labeled as PI/Feac/Coac.

Synthesis of polyimide-based porous carbon/FeC_3 nanoparticles composites (PIC/Fe_3C-1, PIC/Fe_3C-2) and porous carbon/FeCo alloy nanoparticles composites (PIC/FeCo)

To obtain polyimide-based porous carbon, the as-prepared porous PI composite membrane (PI/Feac-1, PI/Feac-2 and PI/Feac/Coac) was calcined in a tubular furnace under the flow of argon gas under specific heating conditions (350–1000 °C, 5 °C/min; 1000 °C/1 h). Thus, obtained composites was labeled PIC/Fe_3C-1, PIC/Fe_3C-2 and PIC/FeCo, respectively. The whole synthetic route of polyimide-based porous carbon/Fe_3C and FeCo alloy nanoparticles composites was schematically illustrated in Scheme 1.

Measurements

The chemical structures of samples were analysed using X-ray powder diffraction (XRD, D/MAX-UltimaIV, Cu Kα, 10–80°, 10° per min), Raman spectroscopy (LabRAM HR Evolution, 523 nm laser), Fourier transform infrared spectroscopy (FT-IR, Nicolet6700), X-ray Photoelectron Spectroscopy (Thermo Scientific K-Alpha) and energy-dispersive X-ray spectroscopy (EDS, Oxford X-Max system). The magnetic properties were measured using a vibrating sample magnetometer (VSM, Lake Shore 7404, 298 K).

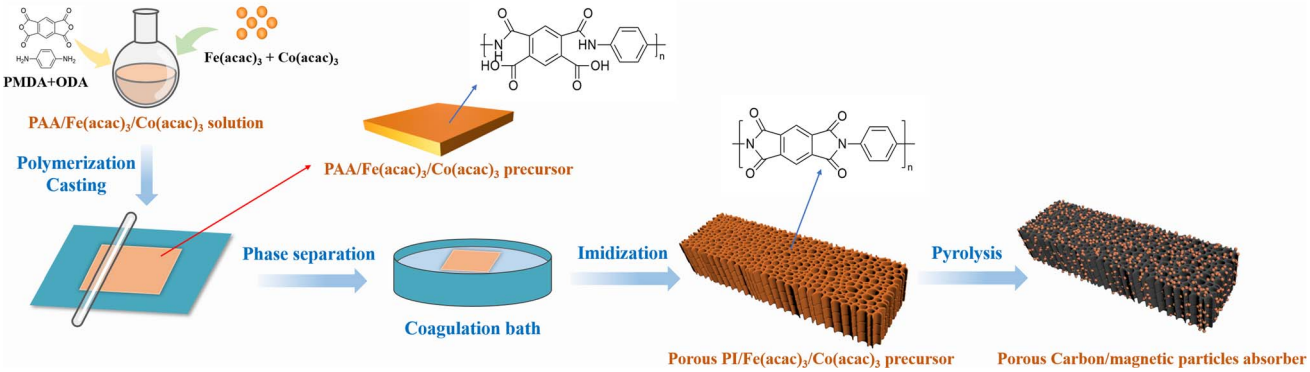

Scheme 1 Synthetic route for the polyimide-based porous carbon/Fe_3C and FeCo alloy nanoparticles composite (PIC/Fe_3C-1, PIC/Fe_3C-2 and PIC/FeCo).

The thermal properties of samples were investigated using thermogravimetric analysis (TGA, PerkinElmer, heating rate: 10 °C per min; gas flow: 50 ml min^{-1}). The morphology of synthesized materials was determined using scanning electron microscopy (SEM, Nova Nano 450). The electromagnetic parameters (complex permeability and permittivity) were measured using a network analyser (N5244A PNA-X, Agilent, toroidal-shaped samples with 25 wt% of products in a paraffin wax matrix, coaxial waveguide method, frequency range: 2–18 GHz).

Results and discussion

Preparation of materials

A one-step strategy has been developed to fabricate a composite electromagnetic wave (EMW) absorber, incorporating polyimide-based porous carbon and FeC_3 nanoparticles. This method involves integrating the liquid–liquid phase separation technique with a pyrolysis process. Illustrated in Scheme 1, the synthesis of the porous carbon/magnetic composite involves using a porous polymer membrane containing PI as the carbon source and $Fe(acac)_3$, $Co(acac)_3$ as the sources of magnetic nanoparticles.

During the imidization process, the complete conversion of PAA to PI was confirmed according to the FT-IR spectra shown in Fig. S1.† Additionally, the TGA curves of PI from 30 °C to 800 °C are presented in Fig. S2.† To verify alterations in the $Fe(acac)_3$ and $Co(acac)_3$, the XRD pattern was acquired and presented in Fig. 1(a). After pyrolysis at 1000 °C, the PI underwent carbonization, All PIC exhibit a diffraction peak at 23°–27°, ascribed to the (002) plane of carbon (PDF: 75-0444). However, the prominent peak at $2\theta = 26.51°$ also can be detected for PIC/Fe_3C-1, PIC/Fe_3C-2 and PIC/FeCo, which may be caused by the catalysis of the Fe_3C and FeCo. For PIC/Fe_3C-1, PIC/Fe_3C-2, the characteristic peaks were consistent with the orthorhombic Fe_3C (PDF: 35-0772). For PIC/FeCo, the characteristic peaks at 44.82°, 56.26°are associated with the (110), (200) planes of the FeCo alloy nanoparticles.

Therefore, it can be affirmed that the $Fe(acac)_3$ and $Co(acac)_3$ underwent chemical reduction to form Fe_3C and FeCo nanoparticles during the carbonization process at 1000 °C. Moreover, the graphitization peaks in the range of 23°–27° are blunter in PIC compared to PIC/Fe_3C and PIC/FeCo. This suggests a relatively high degree of graphitization in PIC/Fe_3C and PIC/FeCo. This observation is further supported by the

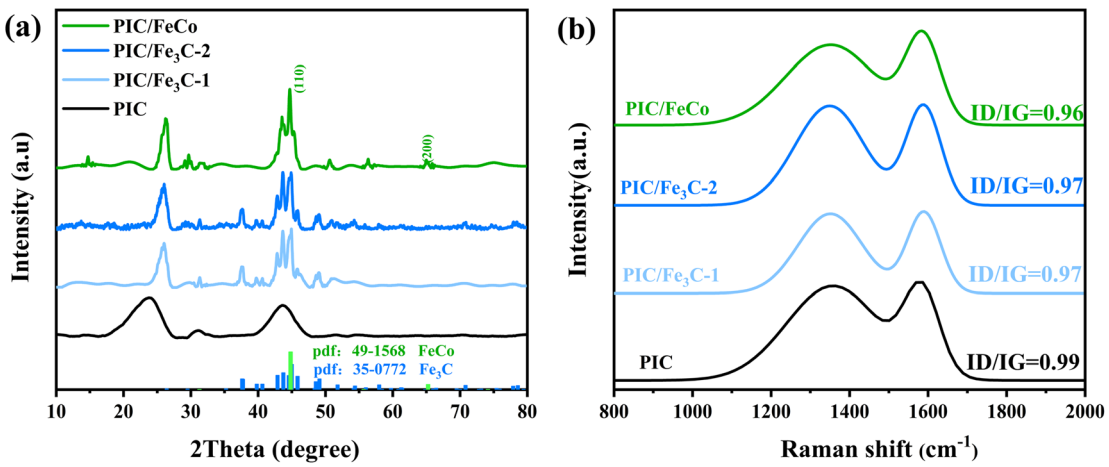

Fig. 1 (a) XRD patterns of PIC, PIC/Fe_3C, and PIC/FeCo; (b) Ramen spectra of PIC, PIC/Fe_3C, and PIC/FeCo.

Raman spectra presented in Fig. 1(b). The prominent peaks in the Raman spectra at around 1360 cm^{-1} and 1590 cm^{-1} are attributed to the D and G bands of carbonaceous materials. The intensity ratio of the D/G bands for PIC, PIC/Fe_3C-1, PIC/Fe_3C-2, PIC/FeCo is 0.99, 0.97, 0.97, 0.96 respectively. Compared with PIC, PIC/Fe_3C-1, PIC/Fe_3C-2 and PIC/FeCo had a lower intensity ratio of the D/G bands, inferring that the intact crystalline phase of Fe_3C and FeCo alloy can catalyse the graphitization and the result agrees with that obtained from the XRD.

XPS was employed to analyse the surface element composition and valence state of PIC/Fe_3C-1. The XPS survey spectrum (Fig. 2(a)) illustrates the presence of C, N, O, and Fe elements. As shown in Fig. 2(b), both samples exhibit two peaks at 284 and 533 eV, corresponding to C and O elements, respectively. The valence states of Fe elements in the PIC/Fe_3C-1 and PIC/Fe_3C-2 were analysed by high-resolution XPS spectroscopy in detail. As shown in Fig. 2(c), the Fe 2p spectrum of PIC/Fe_3C-1 was mainly deconvoluted into two peaks located at 724.9 and 710.9 eV attributed to Fe $2p^{1/2}$ and Fe $2p^{3/2}$, respectively. The devolution of Fe2p spectrum shows the coexistence of three Fe species. Fe^0 with binding energies at 707.5 eV, Fe^{2+} with binding energies at 724.9 and 711.0 eV, and Fe^{3+} with binding energies at 727.0 and 714.1 eV. In addition, PIC/Fe_3C-2 shows XPS spectra like PIC/Fe_3C-1, indicating that the valence states of C and Fe elements in them are basically the same (Fig. S4†). For PIC/FeCo, as shown at Fig. 1(e) The Co 2p spectrum in Fig. 2(e) exhibits two multi-peaks, corresponding to Co $2p^{1/2}$ and Co $2p^{3/2}$ respectively. Further, the peak at 778.5 eV is identified as Co^0; the $Co2p^{3/2}$ peak at 780.7 eV and $Co2p^{1/2}$ peak at 795.8 eV are identified as Co^{2+}; the Co $2p^{3/2}$ peak at 784.7 eV and Co $2p^{1/2}$ peak at 799.5 eV are identified as Co^{3+}. Meanwhile, two multi-peaks of Fe exist in PIC/FeCo (Fig. 2(f)). The Fe $2p^{3/2}$ peaks at 707.3 eV and Fe $2p^{1/2}$ at 720.1 eV belong to Fe^0; the peaks at 709.4 and 722.1 eV are associated with Fe^{2+}. While the broad peaks at 711.1 and 724.1 eV are assigned to Fe^{3+}. The coexistence of Fe and Co elements should originate from the surface oxidation of FeCo alloy in PIC/FeCo.

To characterize the magnetism of PIC/Fe_3C, and PIC/FeCo, the M–H loops of PIC, PIC/Fe_3C were obtained and are shown in Fig. 3(b). The S-like shape with nonzero coercivity (Hc) and remanent magnetization (Mr) demonstrated that PIC/FeCo (Ms: 28.9 emu g^{-1}) maintains the paramagnetic property of the FeCo nanoparticles. Besides, PIC/Fe_3C-1 (Mr: 7.8 emu g^{-1}; Hc:837 Oe) and PIC/Fe_3C-2 (14.5 emu g^{-1}; Hc:561 Oe) shown lower Mr and higher Hc. The high Hc represents a strong magnetic hysteresis behaviour which makes a great contribution to the magnetic loss. When meeting with an incident EMW, the PIC/Fe_3C can create a reversed in-build magnetic field to hinder the change of the external magnetic field and then transform EMW energy to heat or other types of energy. Their lower Ms may be caused by the doping of carbon atoms in Fe and the low content of Fe_3C particles. As the TGA curves shown at Fig. 3(a), under an air atmosphere, the carbon and Fe_3C nanoparticles in PIC/Fe_3C, translates into CO_2, Fe_2O_3 respectively. The weight ratio of Fe_3C is calculated as follows:

$$W_{Fe_3C} = \frac{3}{2}\frac{M_{Fe_3C}}{M_{Fe_2O_3}} \times W_{Fe_2O_3} \quad (1)$$

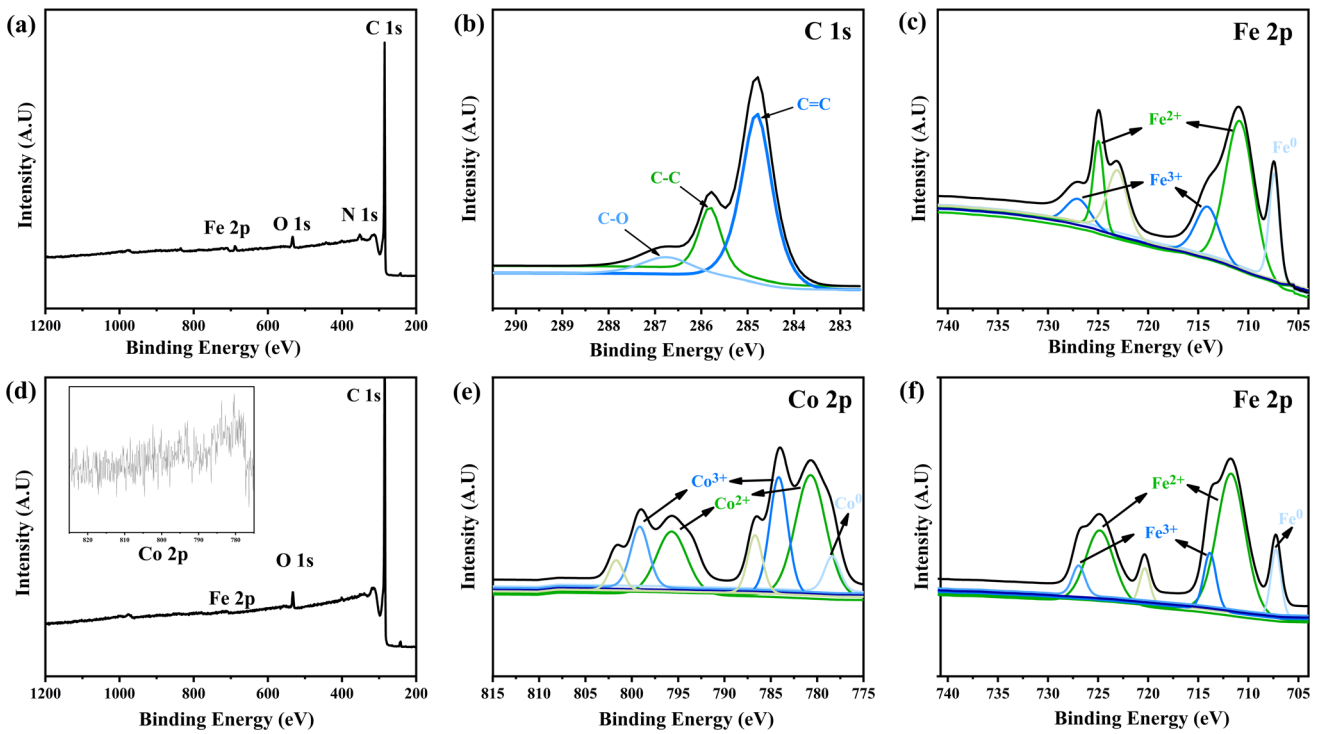

Fig. 2 (a) XPS survey spectrum of PIC/Fe_3C-1; (b) C 1s spectrum; (c) Fe 2p spectrum; (d) XPS survey spectrum of PIC/FeCo; (e) Co 2p spectrum; (f) Fe 2p spectrum.

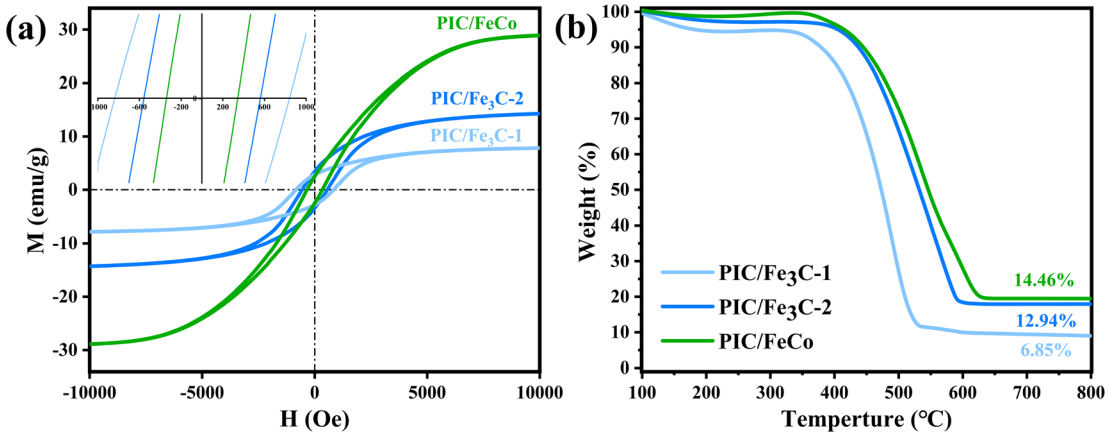

Fig. 3 (a) M–H loops of PIC/Fe_3C, and PIC/FeCo; (b) TGA curves of PIC/Fe_3C-1, PIC/Fe_3C-2 and PIC/FeCo.

where MFe_3C and MFe_2O_3 represent the relative molecular mass of Fe_3C and Fe_2O_3, respectively; WFe_2O_3 refer to residual weight shown in TGA curves. As the residual weight of PIC/Fe_3C-1, PIC/Fe_3C-2 are 6.85%, 12.94%, the Fe_3C particles content in PIC/Fe_3C-1, PIC/Fe_3C-2 were 11.57% and 21.86% according to the weight ratio equation, respectively.

Morphology and porous structure analysis

The microstructure and morphology of the as-synthesized PIC/Fe_3C, PIC/FeCo, and their precursor porous PI membrane were characterized using SEM, with the results presented in Fig. 4. As depicted in Fig. 4(a) and (b), after liquid–liquid phase separation, and imidization, the porous PI has hierarchical pore structure, including the pores with a diameter of 10–20 μm distributed on the surface of the membrane and the coral-like pores with a diameter of 200–600 nm distributed inside the PI membrane After carbonization in 1000 °C, PIC exhibited slight pore collapse and well-defined network structure (Fig. 4(c)). This suggests that the higher glass transition temperature and thermal degradation temperature of PI mitigated the impact of carbonization on the pore structure compared to other polymers. As shown in Fig. 4(d–f) the Fe_3C nanoparticles with a size of about 200 nm were growing on the edge of the hole, the interface between them is difficult to distinguish in the PIC/Fe_3C and PIC/FeCo, which may increase contact area between PIC and Fe_3C/FeCo to improve interface polarization. Further, Fig. 4(g) and (h) shows the elemental mapping images of PIC/Fe_3C-1, PIC/FeCo. Notably, Fe_3C and FeCo alloy nanoparticles are uniformly dispersed on the surface of the carbon skeleton in a cluster morphology, which increases the contact area between carbon skeleton and nanoparticles, resulting in stronger interface polarization.

Electromagnetic absorption properties

To clarify the electromagnetic wave (EMW) absorption capabilities of the PIC/Fe_3C-1, PIC/Fe_3C-2 and PIC/FeCo absorber and the impact of proportion and types of nanoparticles on the EMW absorption properties, the electromagnetic parameters of PIC/Fe_3C-1, PIC/Fe_3C-2 and PIC/FeCo were assessed using complex permittivity and complex permeability, as illustrated in Fig. 4. The real part (ε', μ') of complex permittivity ($\varepsilon_r = \varepsilon' - i\varepsilon''$), complex permeability ($\mu_r = \mu' - i\mu''$) are associated with the storage capacity of electromagnetic energy, while the imaginary parts (ε'' and μ'') signify the loss of electromagnetic energy.[33] As shown in Fig. 5(a–c), PIC/Fe_3C-1, PIC/Fe_3C-2 and PIC/FeCo have high complex permittivity values, both real and imaginary. Due to the low content of Fe_3C, PIC/Fe_3C-1 exhibited lower ε' and ε'' (ε': 12.66–8.74; ε'': 4.59–2.73). Besides, for PIC/Fe_3C-1 (ε': 15.20–9.25; ε'': 7.03–3.87) and PIC/FeCo (ε': 14.85–9.28; ε'': 6.89–3.78), they have similar the complex permittivity values, indicating a relatively stronger dielectric loss performance. Meanwhile, Fig. 5(d–f) depicts PIC/Fe_3C-1, PIC/Fe_3C-2and PIC/FeCo have similar μ' (approximated 1.01–1.00). Especially, PIC/Fe_3C-1 had biggest μ'' (0.0378), This is due to the low content of Fe_3C.

Dielectric tangent loss ($\tan\delta\varepsilon = \varepsilon''/\varepsilon'$) and magnetic tangent loss ($\tan\delta\mu = \mu''/\mu'$) are common parameters that characterize the dielectric and magnetic loss abilities of EMW absorbers. As depicted in Fig. 6(a–c), the variations in $\tan\delta\varepsilon$ and $\tan\delta\mu$ are closely associated with ε'' and μ'', respectively. Considering the relationship of absorption properties with $\tan\delta\varepsilon$ and $\tan\delta\mu$, higher $\tan\delta\varepsilon$ values imply a significant contribution of dielectric loss to the absorption property in both samples. However, the role of magnetic particles as additional promoters for achieving better impedance matching is noteworthy, contributing to the overall EMW absorption performance.

To understand the effect of Fe_3C and FeCo alloy, the dielectric loss mechanisms of PIC/Fe_3C-1, PIC/Fe_3C-2 and PIC/FeCo was evaluated using the Cole–Cole plots, as shown in Fig. 6(d–f). The presence of a straight line at the end of all three Cole–Cole curves indicates the existence of conductance loss during the microwave absorption process, aside from polarization relaxation processes. Furthermore, for PIC/Fe_3C-1, PIC/Fe_3C-2, and PIC/FeCo, the Cole–Cole curves exhibited several deformed semicircles, indicating the presence of Debye relaxation, interface polarization, and dipole polarization in the absorption process.

The reflection factor (RL), as a function that can directly characterize the EMW absorption performance of PIC/Fe_3C-1, PIC/

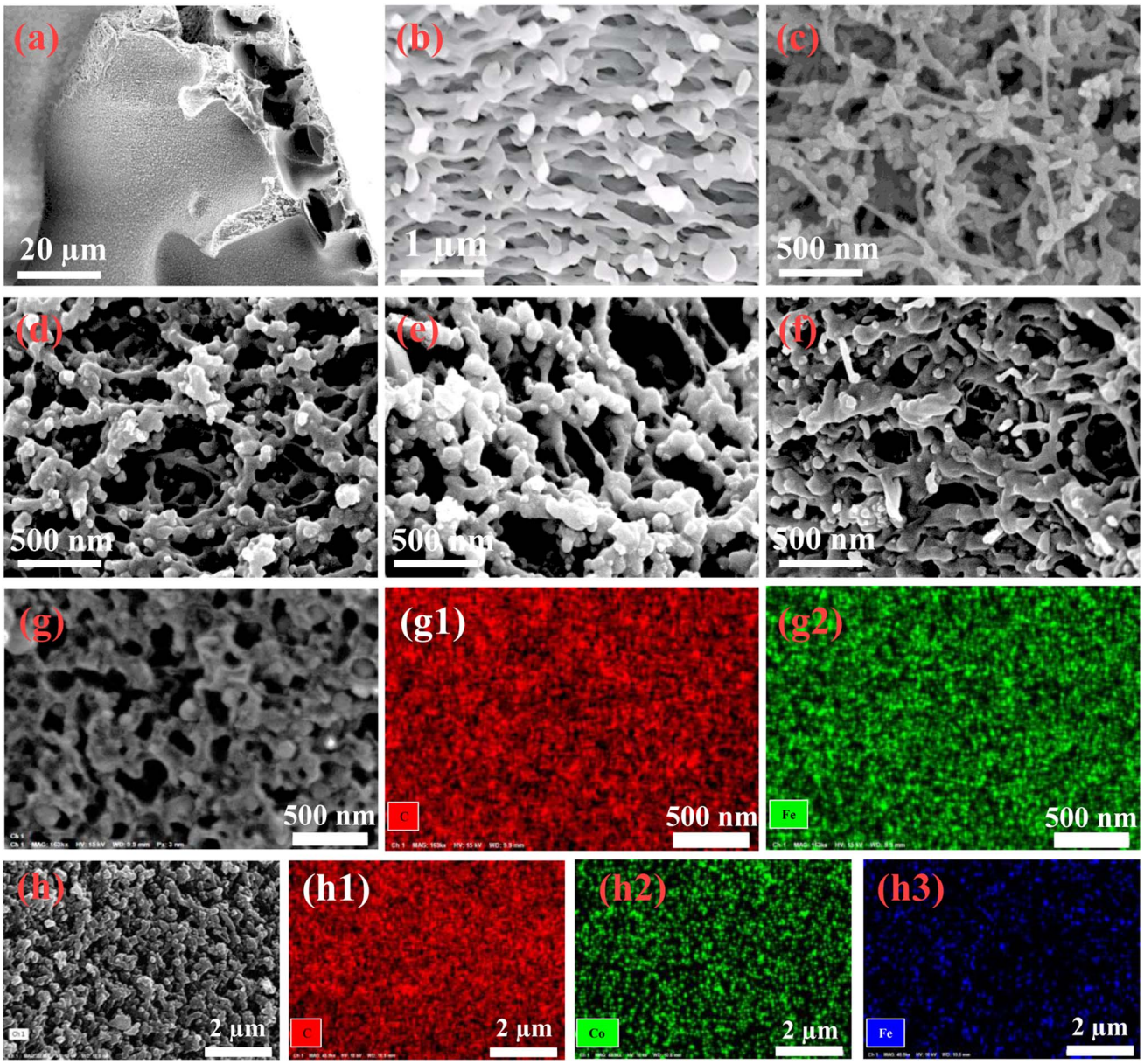

Fig. 4 (a and b) SEM images of porous PI membrane; (c–f) SEM images of PIC(c); PIC/Fe_3C-1, PIC/Fe_3C-2 (d and e) and PIC/FeCo (f); EDS mapping of PIC/Fe_3C-2 (g) and PIC/Fe_3C-2 (h).

Fe_3C-2 and PIC/FeCo, theoretically derived from obtained electromagnetic parameters. According to the transmission line theory, RL can be calculated using the following eqn (2) and (3).[34,35]

$$RL = 20\lg|(Z_{in} - Z_0)/(Z_{in} + Z_0)| \quad (2)$$

$$Z_{in} = Z_0\sqrt{\mu_r/\varepsilon_r}\tanh\left[j(2\pi fd/c)\sqrt{\mu_r/\varepsilon_r}\right] \quad (3)$$

where Z_{in} represents the equivalent input resistance of the sample; Z_0 represents the impedance of free space, is equal to 377 Ω. The μ_r and ε_r are the complex permeability and complex permittivity of the sample, and the c is the speed of light in vacuums. f is the frequency; d is the thickness of the specimen.

The RL values and processing results of PIC illustrate almost no absorption ability due to RL values under different thicknesses that are beyond −10 dB (Fig. S3†). Besides, PIC/Fe_3C-1 with 4.50 mm thickness obtain minimum reflection loss (RL_{min}) of −23.89 dB at 5.36 GHz and effective absorption bandwidth (EABW, the RL < −10 dB, more than 90% EMW absorption) of 3.84 GHz at 1.75 mm (Fig. 7(a)). By comparison, PIC/Fe_3C-2 and PIC/FeCo display excellent EMW absorption performance in terms of RL and EABW. PIC/Fe_3C-2 with 1.50 mm thickness, has the strongest electromagnetic wave loss ability at 17.04 GHz with RL_{min} of −35.37 dB and EABW is 4.95 GHz in the frequency range of 18.0–13.07 GHz at the thickness of 2.78 mm (Fig. 7(b)), showing a broadband absorption characteristic. Furthermore, PIC/FeCo with 1.63 mm thickness, has the strongest electromagnetic wave loss ability at 17.04 GHz with RL_{min} of −56.32 dB and EABW is 4.95 GHz in the frequency

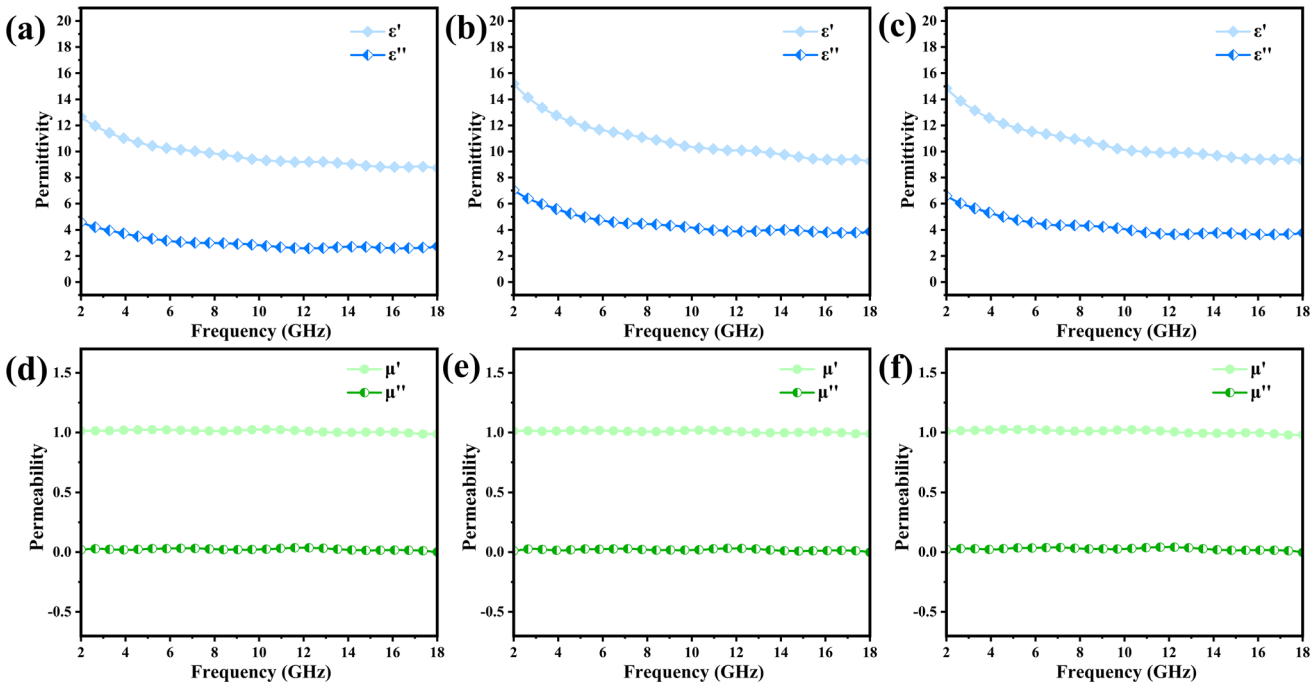

Fig. 5 (a–c) Relative permittivity for PIC/Fe_3C-1, PIC/Fe_3C-2 and PIC/FeCo absorber at 25% absorber content; (d–f) Relative permeability for PIC/Fe_3C-1, PIC/Fe_3C-2 and PIC/FeCo absorber at 25% absorber content.

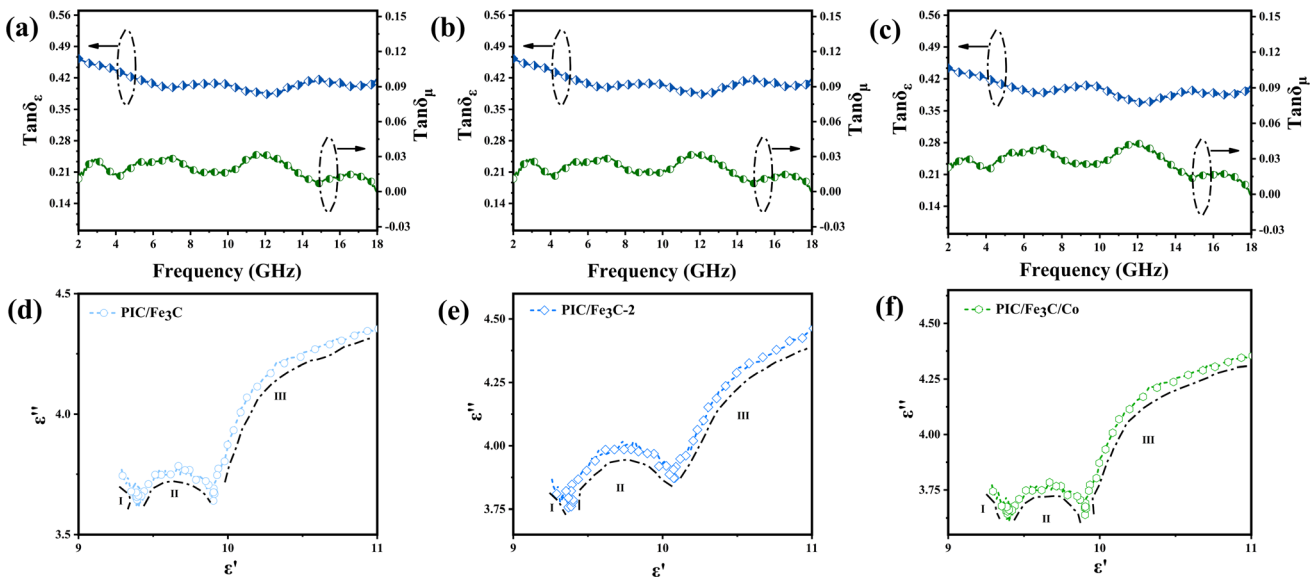

Fig. 6 (a–c) Dielectric tangent loss and magnetic tangent loss of PIC/Fe_3C-1, PIC/Fe_3C-2 and PIC/FeCo absorber at 25% absorber content; (d–f) typical Cole–Cole semicircles ε'' *versus* ε' of PIC/Fe_3C-1, PIC/Fe_3C-2 and PIC/FeCo absorber at 25% absorber content.

range of 18.0–13.07 GHz at the thickness of 2.78 mm (Fig. 7(c)), thus, the incident EMW can be effectively attenuated and transformed into heat and other forms of energy by PIC/Fe_3C-2 and PIC/FeCo.

Following the single-layer homogeneous absorber model,[36] The incident electromagnetic wave that is about to come into contact with the surface of the absorber layer has three directions for its electromagnetic energy (E0) after entering the interior of the absorber layer: Part of E0 reflects on the surface of the layer (air-absorber interface) and returns to the air again the reflected EMW energy on the (E1); Attenuation after entering the interior of absorber the and interacting with it (E2); and the final EMW energy penetrating the absorber layer and re-reflecting on the surface of the metal layer (the absorber-metal interface (E3). Specifically, when the absorption layer has an appropriate thickness, *i.e.* a quarter of the incident wavelength

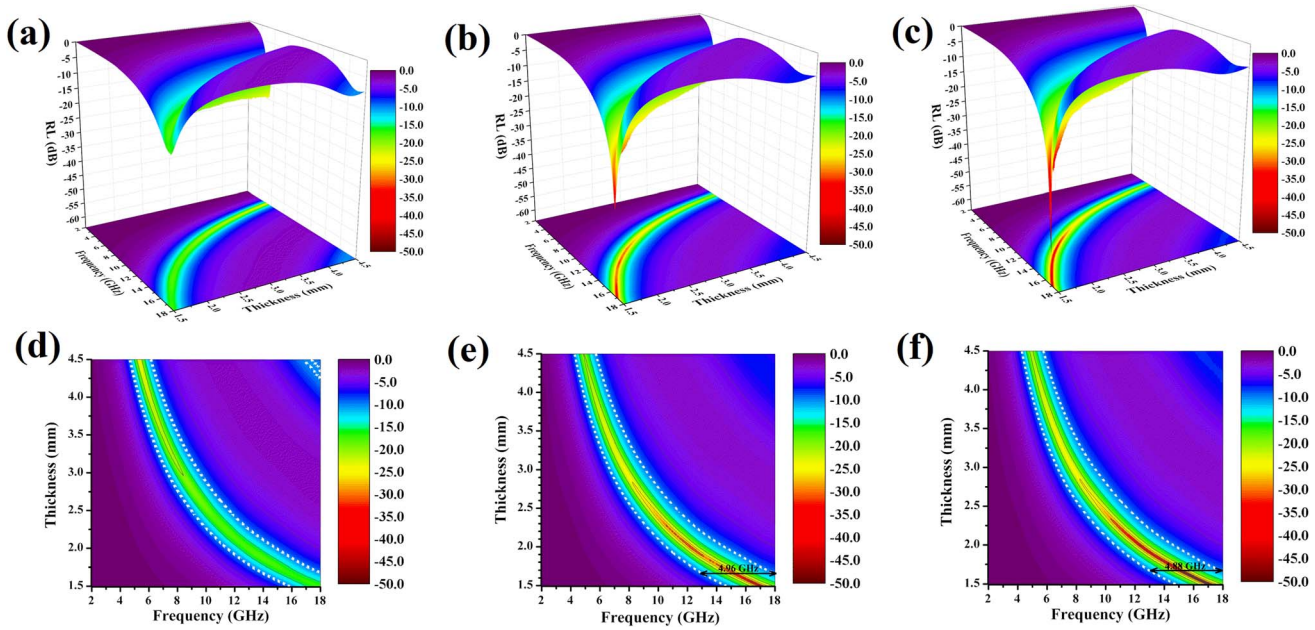

Fig. 7 3D Reflection loss and 2D projection plots of PIC/Fe_3C-1 (a and d), PIC/Fe_3C-2 (b and e) and PIC/FeCo (c and f).

frequency, the phase difference between E1 (incident from air-absorber interface) and E3 (ejection from absorber-metal interface) is exactly 180°, so the electromagnetic wave energy of the two can nullify each other. This phenomenon is widely known as the quarter-wavelength cancellation model. Consequently, the absorber layer at a specific thickness (t_m) can achieve minimal reflection at a certain EMW frequency (f_m). The mathematical relationship between tm and fm satisfy the following eqn (4).[37]

$$t_m = \frac{nc}{4f_m\sqrt{|\mu_r||\varepsilon_r|}}(n = 1, 3, 5\ldots) \quad (4)$$

where the f_m is the frequency corresponding to obtaining the RL_{min} value.

The model portrays the inverse relation between the peak frequency and the absorber layer's thickness. As shown in Fig. 8(b) and (e), It is expected that all thickness related to RL_{min} value (red symbols) are located around the blue line (the 1/4 wavelength curve of the peak frequency). Consequently, the PIC/Fe_3C-2 and PIC/FeCo obeys the quarter-wavelength cancellation model, and thus can be concluded that PIC/Fe_3C-2 and PIC/FeCo has considerable contributions to the EMW attenuation performance.

Besides, to obtain the excellent EMW absorption performance, reducing the reflection of EMW (E1) at the air-absorber interface and improving the absorption of the incident EMW (E2) in the absorber layer with a low reflection at the absorber-metal interface (E3) is necessary. The impedance matching characteristics (Z) is an important parameter for reducing the reflection of EMW at the air-absorber interface and is expressed in the following eqn (5).[38]

$$Z = |Z_{in}/Z_0| = \sqrt{\mu_r/\varepsilon_r}\tanh\left[j(2\pi fd/c)\sqrt{\mu_r/\varepsilon_r}\right] \quad (5)$$

When the values of Z_{in} and Z_0 are approximately equal, indicating a Z value close to 1, most EMW are absorbed by the surface of the absorber rather than being reflected.[39,40] The frequency dependence of Z for PIC/Fe_3C-2 and PIC/FeCo is shown in Fig. 8(c and f). For PIC/Fe_3C-2 and PIC/FeCo, at thicknesses of 1.50 (1.96) and 1.63 mm in the absorber layer, respectively, Z is 0.974 (0.948) and 0.997 at 16.96 (12.48) and 15.6 GHz, respectively. Simultaneously, these frequencies correspond to the observation of a RL_{min}. Interestingly, the porous structures are equivalent to introducing dispersed phases (air) into a continuous phase (carbon), which helps decrease the effective permittivity while balancing permittivity and permeability. Consequently, EMW can easily penetrate the absorber and undergo attenuation rather than reflecting at the absorber surface. Moreover, the well-tuned impedance matching condition of PIC/Fe_3C-2 and PIC/FeCo contributes to its outstanding absorbing performance. Attenuation constant (α) is an important parameter which determines the attenuation characteristics of the absorber directly. α can be calculated using the following eqn (6).[41] As shown in Fig. S5,† the α values of PIC/Fe_3C-1, PIC/Fe_3C-2 and PIC/FeCo show an increasing trend with increasing frequency from 2 GHz to 18 GHz. The α value of PIC/Fe_3C-2 (233.3) and PIC/FeCo (225.2) are higher than PIC/Fe_3C-1 (172.3), indicating that they have stronger EMW attenuation capability. However, though PIC/Fe_3C-2 has higher α than PIC/FeCo, PIC/FeCo has better impedance matching, which ensure better EMW absorption and dissipation.

$$\alpha = \frac{\sqrt{2}\pi f}{c}\sqrt{(\mu''\varepsilon'' - \mu'\varepsilon') + \sqrt{(\mu''\varepsilon'' - \mu'\varepsilon')^2 + (\mu'\varepsilon'' + \mu''\varepsilon')^2}} \quad (6)$$

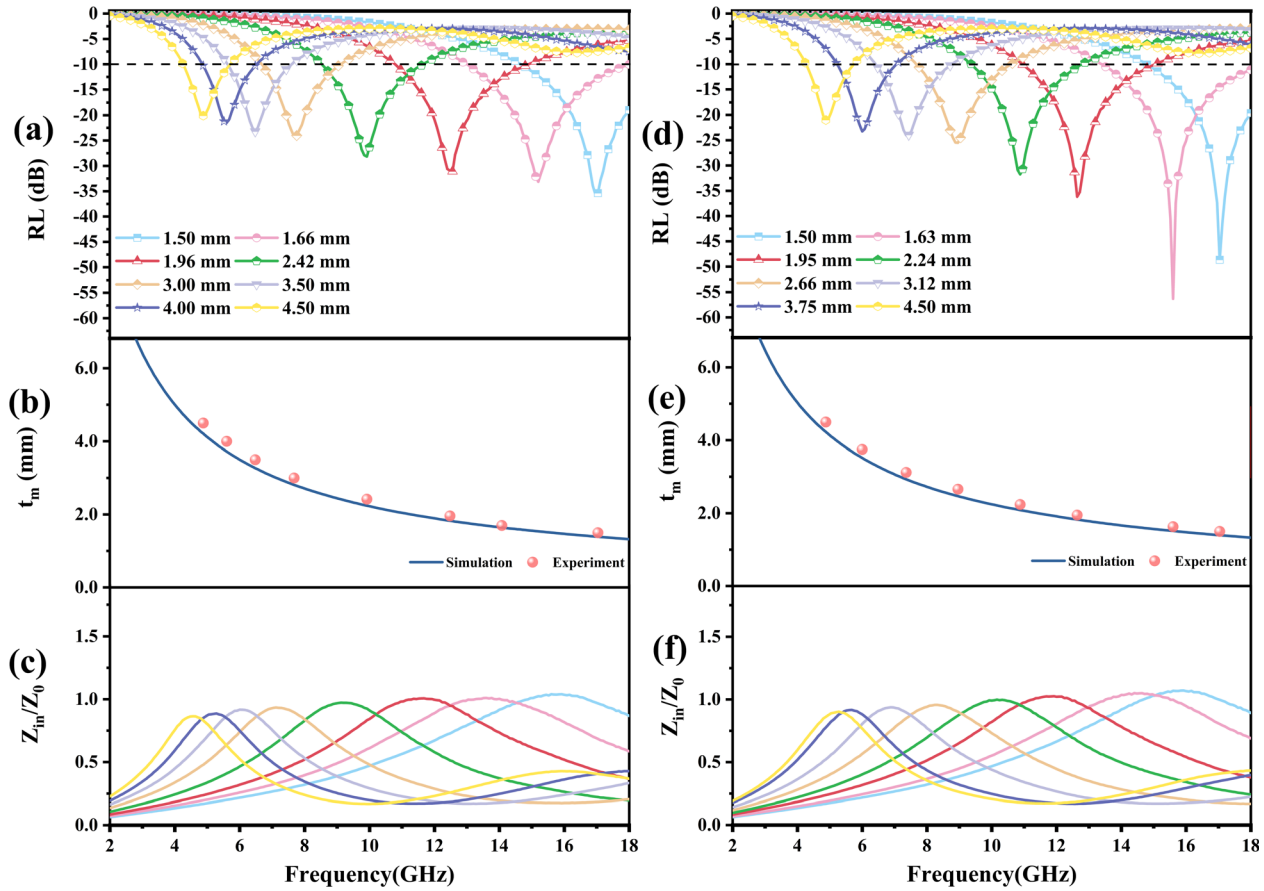

Fig. 8 RL curves with different thicknesses of PIC/Fe_3C-2 (a) and PIC/FeCo (d); simulated and experimental values under 1/4 wavelength matching conditions of PIC/Fe_3C-2 (b) and PIC/FeCo (e); impedance matching characteristics values of PIC/Fe_3C-2 (c) and PIC/FeCo (f).

Shown in Fig. 9, The EMW absorption mechanism of PIC/Fe_3C-2 and PIC/FeCo can be explained in the following parts. Based on the coexistence of the dielectric material PIC and magnetic nanoparticles Fe_3C and FeCo alloy, dissipation of incident EMW mainly includes dielectric loss and magnetic loss.[42,43] The dielectric loss is manifested in dipole polarization, defect polarization and interface polarization. First, there are residual oxygen and nitrogen atoms on the surface of PIC

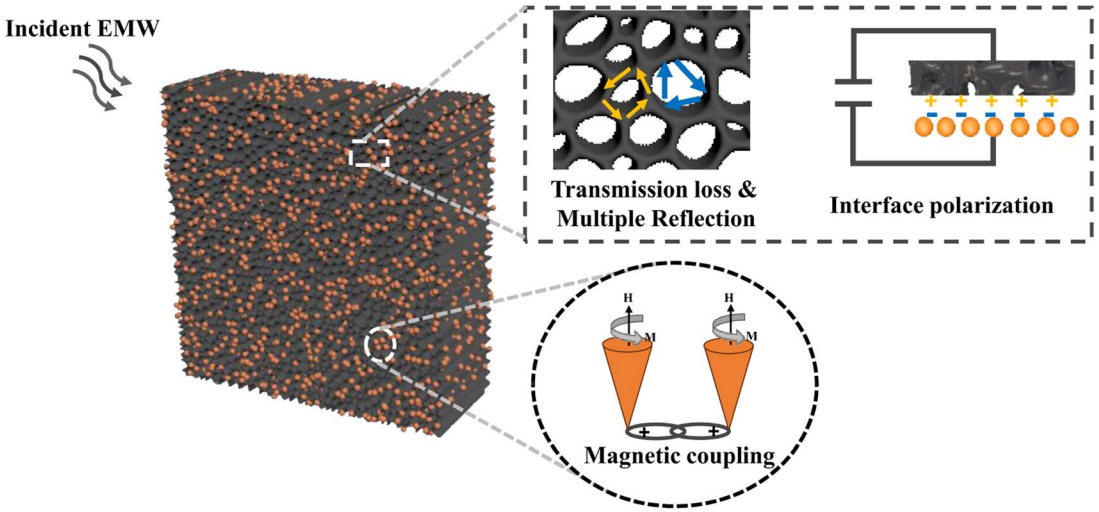

Fig. 9 The schematic presentation of microwave absorbing mechanism of PIC/Fe_3C-2 and PIC/FeCo.

during carbonization, which changes the distribution of electric clouds to the formation of Electric dipoles to distinct EWM. Second, pores (air) in porous carbon can also be considered as a special defect which sites in absorbers can trap charge carriers and break the balance of charge distribution, thus leading to the polarization process and corresponding EMW energy loss. Third, pore (air), PIC matrix and Fe_3C/FeCo alloy nanoparticles constructs a multiple heterointerfaces. Specifically, as a special type of iron/carbon hybrid material, Fe_3C can provide more interfaces than carbon/single magnetic materials (metals), causing strong interface polarization and dielectric relaxation. Additionally, the mismatched electronegativity between PIC and Fe_3C/FeCo alloy nanoparticles enhances interface polarization. Further, the multiple reflection inside the coral-like pore structure of PIC may result in extended more propagation path for incident EMW, which are converted into heat or other energy for further dissipation. Thereby achieving improved EMW attenuation capability of PIC.[44] In addition to dielectric loss, magnetic Fe_3C and FeCo alloy nanoparticles also contribute to natural resonance, exchange resonance, and eddy current effects, enhancing magnetic loss.

Conclusions

In summary, we successfully utilized a straightforward approach, choosing liquid–liquid phase separation to build a porous structure and synthesize composite absorbers based on polyimide-based porous carbon/Fe_3C nanoparticles and porous carbon/FeCo alloy nanoparticles. The specially designed coral-like pore structures were observed to enhance impedance matching, contribute multiple reflection and strong interfacial polarization, significantly contributes to enhanced EMW absorption. Importantly, the co-existence of Fe_3C and FeCo alloy nanoparticles not only induces magnetic loss but also enhances the composite's interface polarization, thus further enhancing the electromagnetic wave attenuation effect of the PIC absorbers through catalytic carbonization.

At thicknesses of 4.50 mm, PIC/Fe_3C-1 achieves RL_{min} values of −23.89 dB, with EABW of 3.84 GHz. By adding the content of Fe_3C, PIC/Fe_3C-2 obtained RL_{min} of −35.37 dB at 17.04 GHz with 1.55 mm thickness and EABW of 4.95 GHz with 1.66 mm thickness. Furthermore, PIC/FeCo with 1.63 mm thickness, has the strongest electromagnetic wave loss ability at 15.6 GHz with RL_{min} of −56.32 dB and EABW is 4.88 GHz. Thus, the design strategy presented in this study could serve as a model for synthesizing other high-performance absorbers, effectively mitigating electromagnetic wave-induced pollution.

Conflicts of interest

There are no conflicts to declare.

Acknowledgements

The authors gratefully acknowledge the National Key R&D Program of China (No. 2020YFB0408100), Guangdong Innovative and Entrepreneurial Research Team Program (No. 2016ZT06C412), National Natural Science Foundation of China (NSFC; No. U20A20340).

References

1 Z. Jia, D. Lan, K. Lin, M. Qin, K. Kou, G. Wu and H. Wu, *J. Mater. Sci.: Mater. Electron.*, 2018, **29**, 17122–17136.
2 X. Chen, H. Liu, D. Hu, H. Liu and W. Ma, *Ceram. Int.*, 2021, **47**, 23749–23761.
3 Q. Xia, Z. Han, Z. Zhang, Z. Huang, X. Wang, J. Chang, Q. Chen and M. Chen, *J. Mater. Chem. C*, 2023, **11**, 4552–4569.
4 W. T. Cao, F. F. Chen, Y. J. Zhu, Y. G. Zhang, Y. Y. Jiang, M. G. Ma and F. Chen, *ACS Nano*, 2018, **12**, 4583–4593.
5 O. P. Gandhi, *Annu. Rev. Biomed. Eng.*, 2002, **4**, 211–234.
6 C.-J. Li, X. Wang, X. Liu, J. Zhang, S. Bi and Z.-L. Hou, *Carbon*, 2023, 214.
7 W.-y. Li, M.-y. Gao, Y. Miao and X.-m. Wang, *New Carbon Mater.*, 2023, **38**, 111–125.
8 S. Hui, X. Zhou, L. Zhang and H. Wu, *Adv. Sci.*, 2023, e2307649, DOI: **10.1002/advs.202307649**.
9 Q. Wang, J. Liu, Y. Li, Z. Lou and Y. Li, *Int. J. Miner., Metall. Mater.*, 2023, **30**, 446–473.
10 Y. Han, M. He, J. Hu, P. Liu, Z. Liu, Z. Ma, W. Ju and J. Gu, *Nano Res.*, 2022, **16**, 1773–1778.
11 N. Poudyal, C. Rong, Y. Zhang, D. Wang, M. J. Kramer, R. J. Hebert and J. Ping Liu, *J. Alloys Compd.*, 2012, **521**, 55–59.
12 R. Han, W. Li, W. Pan, M. Zhu, D. Zhou and F. S. Li, *Sci. Rep.*, 2014, **4**, 7493.
13 X. Li, Y. Sun, Y. Zong, Y. Wei, X. Liu, X. Li, Y. Peng and X. Zheng, *J. Alloys Compd.*, 2020, **841**, 155710.
14 X. Liu, C. Hao, H. Jiang, M. Zeng and R. Yu, *J. Mater. Chem. C*, 2017, **5**, 3770–3778.
15 M. Ma, W. Li, Z. Tong, W. Huang, R. Wang, P. Lyu, Y. Ma, G. Wu, Q. Yan, P. Li and X. Yao, *J. Alloys Compd.*, 2020, **843**, 155199.
16 W. Zhu, L. Wang, R. Zhao, J. Ren, G. Lu and Y. Wang, *Nanoscale*, 2011, **3**, 2862–2864.
17 T. Zhao, C. Hou, H. Zhang, R. Zhu, S. She, J. Wang, T. Li, Z. Liu and B. Wei, *Sci. Rep.*, 2014, **4**, 5619.
18 L. Kong, X. Yin, H. Xu, X. Yuan, T. Wang, Z. Xu, J. Huang, R. Yang and H. Fan, *Carbon*, 2019, **145**, 61–66.
19 Z. Wang, Y. Min, J. Fang, W. Yu, W. Huang, X. Lu and B. Wang, *RSC Adv.*, 2023, **13**, 7055–7062.
20 Z. Zhang, J. W. Tan, W. H. Gu, H. Q. Zhao, J. Zheng, B. S. Zhang and G. B. Ji, *Chem. Eng. J.*, 2020, **395**, 125190.
21 F. Ruiz-Perez, S. M. López-Estrada, R. V. Tolentino-Hernández and F. Caballero-Briones, *J. Sci.: Adv. Mater. Devices*, 2022, **7**, 100454.
22 Y. Sun, Y. Wang, H. Ma, Y. Zhou, H. Xing, W. Feng, J. Feng, Z. Shi, Y. Zong, X. Li and X. Zheng, *Carbon*, 2021, **178**, 515–527.
23 D. Wang, J. Jin, Y. Guo, H. Liu, Z. Guo, C. Liu and C. Shen, *Carbon*, 2023, **202**, 464–474.
24 W. Hou, K. Peng, S. Li, F. Huang, B. Wang, X. Yu, H. Yang and H. Zhang, *J. Colloid Interface Sci.*, 2023, **646**, 265–274.

25 Y. Ren, Y. Zhang, Q. Zheng, L. Wang and W. Jiang, *Carbon*, 2023, **206**, 226–236.
26 Q. Li, J. Liu, Y. Zhao, X. Zhao, W. You, X. Li and R. Che, *ACS Appl. Mater. Interfaces*, 2018, **10**, 27540–27547.
27 Z. Zhao, X. Zhou, K. Kou and H. Wu, *Carbon*, 2021, **173**, 80–90.
28 R. Qiang, Y. Du, Y. Wang, N. Wang, C. Tian, J. Ma, P. Xu and X. Han, *Carbon*, 2016, **98**, 599–606.
29 F. E. Elbakoush, D. Yang, S. Qi, M. Zhang, G. Tian, X. Wang and D. Wu, *Polym. Sci., Ser. B*, 2017, **59**, 430–436.
30 S. Kim, J. Son, H. Park, E. Jeong, K. H. Nam and J. S. Bae, *Polymers*, 2022, **14**, 1425.
31 H. Li, X. Kong, S. Wang, M. Gong, X. Lin, L. Zhang and D. Wang, *Molecules*, 2023, **28**, 3095.
32 W. Yu, Y. Min, J. Fang, X. Lu, Z. Wang and L. Jian, *RSC Adv.*, 2022, **12**, 29070–29077.
33 H. Wei, Z. Zhang, G. Hussain, L. Zhou, Q. Li and K. Ostrikov, *Appl. Mater. Today*, 2020, **19**, 100596.
34 Y. Zhan, L. Xia, H. Yang, N. Zhou, G. Ma, T. Zhang, X. Huang, L. Xiong, C. Qin and W. Guangwu, *Carbon*, 2021, **175**, 101–111.
35 M. Zhang, H. Ling, S. Ding, Y. Xie, T. Cheng, L. Zhao, T. Wang, H. Bian, H. Lin, Z. Li and A. Meng, *Carbon*, 2021, **174**, 248–259.
36 J. Fang, Y. Shang, Z. Chen, W. Wei, Y. Hu, X. Yue and Z. Jiang, *J. Mater. Chem. C*, 2017, **5**, 4695–4705.
37 C. Wang, Y. Liu, Z. Jia, W. Zhao and G. Wu, *Nanomicro Lett.*, 2022, **15**, 13.
38 Z. Li, H. Lin, S. Ding, H. Ling, T. Wang, Z. Miao, M. Zhang, A. Meng and Q. Li, *Carbon*, 2020, **167**, 148–159.
39 D. Wu, J. Jiang, S. Deng, Q. He and Y. Wang, *J. Alloys Compd.*, 2023, 963.
40 S. Deng, J. Jiang, D. Wu, Q. He and Y. Wang, *J. Colloid Interface Sci.*, 2023, **650**, 710–718.
41 D. Wu, S. Deng, Y. Wang, J. Wen, L. Ren and Q. He, *Mater. Res. Bull.*, 2024, **172**, 112653.
42 H. Yan, Z. Lou, L. Xu and H. Lv, *Chem. Eng. J.*, 2023, **464**, 142568.
43 Z. Lou, Q. Wang, X. Zhou, U. I. Kara, R. S. Mamtani, H. Lv, M. Zhang, Z. Yang, Y. Li, C. Wang, S. Adera and X. Wang, *J. Mater. Sci. Technol.*, 2022, **113**, 33–39.
44 L. Wang, Z. Ma, H. Qiu, Y. Zhang, Z. Yu and J. Gu, *Nanomicro Lett.*, 2022, **14**, 224.